Research on the Hydrodynamic Characteristics of APFSDS During Underwater Launch with Different Sabot Structures

Tengfei Xu *, Zeqing Guo *, Heng Zhang *, Shuai Sun *and Pengfei Liu **
Corresponding author: guozq@ njust. edu. cn
* Nanjing University of Science and Technology, CN.
** Wuhan University of Technology, CN.

Abstract: Supercavitating projectiles launched underwater offer a promising approach for rapid defense against underwater threats by circumventing the complex hydrodynamic disturbances associated with crossing the air-water interface. However, to achieve both high stability and sufficient terminal effectiveness, such projectiles necessarily adopt a discarding sabot configuration, whose separation behavior critically influences the subsequent flight trajectory. In this study, a numerical framework coupling the Volume of Fluid (VOF) multiphase model, the Schnerr-Sauer cavitation model, the SST k-ω turbulence model, and the classical interior ballistic equations is established to simulate the sealed underwater launch process of an armor-piercing fin-stabilized discarding sabot (APFSDS) projectile. Three sabot geometries—conical, flat-nosed, and chamfered leading-edge—are systematically compared at a muzzle velocity of 605.4 m/s to elucidate their effects on cavity evolution, flow field development, projectile motion, and sabot separation dynamics. The results reveal that the underwater separation process is jointly governed by mechanical and hydrodynamic actions, distinctly differing from that in air. The conical sabot exhibits the lowest drag and the most stable force characteristics but delays separation significantly. The flat-nosed sabot achieves the earliest separation at the cost of severe frontal pressure loads and greater force fluctuations. The chamfered leading-edge sabot strikes a balanced compromise, offering moderately early separation, the slowest velocity attenuation, and alleviated stress concentrations. These findings provide quantitative guidance for sabot geometry optimization in underwater-launched supercavitating projectile design.

Keywords: Underwater launch; Muzzle flow field; APFSDS

1. Introduction

As a hydrodynamic kinetic energy weapon that achieves high-speed, low-drag motion based on cavitation effects, supercavitating projectiles can reach velocities on the order of kilometers per second. When addressing underwater threats, supercavitating projectiles launched across media typically need to enter the water at a small angle and high speed. During this process, disturbances from the muzzle flow field and the external wave environment are unavoidable, subjecting the projectile to asymmetric impact loads. This exacerbates the asymmetry of the cavity shape and may even induce ricochet, affecting strike accuracy and reliability[1-2]. In contrast, underwater launching offers a new approach for the application of supercavitating projectiles. By launching supercavitating projectiles via underwater artillery, the impact of crossing the media interface can be effectively avoided, enabling rapid strikes against underwater targets while circumventing aerial threats to the ammunition. However, the underwater launch environment imposes specific requirements on projectile design: to maintain motion stability, the projectile needs a large length-to-diameter ratio; simultaneously, to ensure damage efficiency, a projectile structure with high specific kinetic energy (i.e., kinetic energy per unit cross-sectional area) must be adopted. Based on ammunition design theory, the discarding sabot structure is the only feasible solution to meet the above performance requirements and has thus become a critical bottleneck in the development of underwater-launched supercavitating projectile technology.

APFSDS primarily consists of penetrator and sabot. The sabot separates after the projectile exits the muzzle, influenced by the combined action of the in-bore propellant gas and the fluid resistance ahead of the projectile. Research indicates that the hydrodynamic effects and mechanical interactions between the sabot and the penetrator during the separation process directly influence the smoothness of sabot separation, subsequently affecting the flight stability, accuracy, and armor-piercing performance of the penetrator. Sangeeta et al.[3] quantified the effects of various factors during the in-bore motion and external ballistic phases on the dispersion of 120 mm armor-piercing projectiles. They found that a reduction in residual spin rate by approximately 5% led to a 56% decrease in the first maximum yaw, indicating a significant correlation between the two. The effectiveness of their proposed design was validated through simulations and flight trials. Acharya et al. [4-5] divided the sabot separation process into four stages based on its characteristics and defined three transition points for theoretical analysis and calculation of each stage. They discussed the influences of mechanical collision, shock waves, aerodynamic forces, propellant gas, and gravity on sabot separation. The results indicated that mechanical collision and aerodynamic forces are the major sources of disturbance to the penetrator. Zhang et al.[6] investigated the influence of spin rate on the sabot discard characteristics of armor-piercing fin-stabilized discarding sabot (APFSDS) projectiles launched from a rifled barrel. Their study revealed that an increase in spin rate exacerbates the asymmetry of sabot discard, thereby altering the relative position between the sabot and the penetrator as well as the surface pressure distribution on the penetrator, which subsequently affects its aerodynamic characteristics. They determined that 1000 rad/s is the optimal spin rate for this type of rifled barrel gun. Huang et al.[7] explored the asymmetric discard behavior of sabots under different angles of attack. They discovered that a larger angle of attack intensifies the asymmetry of sabot discard, resulting in a more complex pressure distribution on the penetrator surface and more drastic changes in aerodynamic forces. Furthermore, this aerodynamic interference has a more pronounced impact on firing accuracy and flight stability as the angle of attack increases.

Based on the aforementioned research background, and to advance the theoretical framework for underwater launched supercavitating projectiles, this paper establishes a numerical simulation method for the underwater launch process of supercavitating projectiles using the Schnerr-Sauer cavitation model and multiphase flow models. It systematically investigates the sealed underwater launch process for three different sabot structures at a muzzle velocity of v_0 = 605.4 m/s. The analysis focuses on cavity evolution characteristics, flow field distribution patterns, projectile motion characteristics, and sabot separation behavior, aiming to provide a reference for trajectory prediction and structural optimization of underwater-launched supercavitating projectiles.

2. Methodology

This study employs the Volume of Fluid (VOF) model to perform numerical simulations of fluid motion:

$$\frac{\partial \rho_{\mathrm{m}}}{\partial t}+\frac{\partial(\rho_{\mathrm{m}} u_{\mathrm{i}})}{\partial x_{\mathrm{i}}}=0$$

$$\frac{\partial}{\partial t}(\rho_{\mathrm{m}} u_{\mathrm{i}})+\frac{\partial}{\partial x_{\mathrm{j}}}(\rho_{\mathrm{m}} u_{\mathrm{i}} u_{\mathrm{j}})=-\frac{\partial p}{\partial x_{\mathrm{i}}}+\mu_{\mathrm{m}} \frac{\partial}{\partial x_{\mathrm{j}}}\left(\frac{\partial u_{\mathrm{i}}}{\partial x_{\mathrm{j}}}+\frac{\partial u_{\mathrm{j}}}{\partial x_{\mathrm{i}}}\right)+\rho_{\mathrm{m}} g_{\mathrm{i}}$$

Where ρ_m is the mixture density; p is the pressure; u_i and u_j are the velocity components in the Cartesian coordinate system; μ_m is the mixture viscosity; g_i is the component of gravitational acceleration; x_i and x_j are the axis coordinate components.

The underwater launch of a supercavitating projectile occurs in an environment characterized by extremely high temperature and pressure. The ideal gas equation of state is employed to describe gas compressibility:

$$p=\rho R T$$

Where R and T are the specific gas constant and temperature, respectively.

The VOF model requires that the sum of the volume fractions of all components within a control volume equals unity, thereby satisfying the conservation equation:

$$\sum_{q=1}^{n}\alpha_{\mathrm{q}}=1$$

The volume fraction of the q-th phase can be expressed as:

$$\frac{\partial}{\partial t}(\alpha_{\mathrm{q}})+\nabla\cdot(\alpha_{\mathrm{q}}\overrightarrow{v_{\mathrm{q}}})=\frac{1}{\rho_{\mathrm{q}}}[S_{\alpha_{\mathrm{q}}}+\sum_{p=1}^{n}(\dot{m}_{\mathrm{pq}}-\dot{m}_{\mathrm{qp}})]$$

Where ρ_q is the density of the q-th phase, α_q is the volume fraction of the q-th phase, $\vec{v}_q$ is the velocity of the q-th phase; $\dot{m}_{pq}$ is the mass transfer rate from the q-th phase to the p-th phase; $\dot{m}_{qp}$ is the mass transfer rate from the p-th phase to the q-th phase.

This study adopts the SST $k-\omega$ model to solve the Reynolds-Averaged Navier–Stokes (RANS) equations for numerical results:

$$\mu_{\mathrm{t}}=\rho_{\mathrm{m}}k\cdot\min(\frac{a^{*}}{\omega},\frac{a_1}{SF_1})$$

Where k is the turbulent kinetic energy; ω is the turbulent dissipation rate; $a^{*}=1$ and $a=1$ are model coefficients; S is the mean strain rate tensor. The blending function F_1 is computed as follows:

$$F_1=\tanh\left\{\left[max\left(\frac{2\sqrt{k}}{\beta^{*}\omega d},\frac{500v}{d^2\omega}\right)\right]^2\right\}$$

Where d is the distance to the nearest wall.

The transport equations for turbulent kinetic energy k and turbulent dissipation rate ω are given by:

$$\frac{\partial}{\partial t}(\rho_{\mathrm{m}}k)+\nabla\cdot(\rho_{\mathrm{m}}k\bar{u})=\nabla\cdot[(\mu_{\mathrm{m}}+\sigma_{\mathrm{k}}\mu_{\mathrm{t}})\nabla k]+P_{\mathrm{k}}-\rho_{\mathrm{m}}\beta^{*}f_{\beta^{*}}(\omega k-\omega_0k_0)$$

$$\frac{\partial}{\partial t}(\rho_{\mathrm{m}}\omega)+\nabla\cdot(\rho_{\mathrm{m}}\omega\bar{u})=\nabla\cdot[(\mu+\sigma_{\omega}\mu_{\mathrm{t}})\nabla\omega]+P_{\omega}-\rho_{\mathrm{m}}\beta f_{\beta}(\omega^2-\omega_0^2)$$

Among them, p_k and p_w are related to specific dissipation, cross-diffusion, turbulence, buoyancy, and nonlinear effects; $f_{\beta*}$ and f_β represent the correction coefficients for free shear and vortex stretching, respectively. Furthermore, σ_k and σ_w are the model coefficients associated with the blending function F_1, and are calculated as follows:

$$\sigma_{\mathrm{k}}=F_2\sigma_{\mathrm{k}_1}+(1-F_2)\sigma_{\mathrm{k}_2}$$

$$\sigma_{\omega}=F_2\sigma_{\omega_1}+(1-F_2)\sigma_{\omega_2}$$

$$F_2=\tanh\left\{\left[min\left(max\left(\frac{\sqrt{k}}{\beta^{*}\omega d},\frac{500v}{d^2\omega}\right),\frac{2k}{d^2CD_{k\omega}}\right)\right]\right\}^4$$

where the coefficients σ_{k1} , σ_{k2} , σ_{w1} , σ_{w2} , CD_{kw}, etc., are the model coefficients.

The Schnerr-Sauer cavitation model is adopted to simulate the cavitation phenomena:

$$\frac{\partial(\rho_v \alpha_v)}{\partial t} + \frac{\partial(\rho_v \alpha_v u_i)}{\partial x_i} = R_e - R_c$$

$$R_e = F_{vap} \frac{3\alpha_{nuc}(1-\alpha_v)\rho_v}{R_B} \sqrt{\frac{2}{3}\frac{(p_v - p)}{\rho_l}}$$

$$R_c = F_{cond} \frac{3\alpha_v \rho_v}{R_B} \sqrt{\frac{2}{3} \cdot \frac{2(p_v - p)}{\rho}}$$

Where R_e and R_c are the evaporation and condensation rates per unit volume, respectively; the evaporation coefficient $F_{vap} = 50$; the nucleation site volume fraction $\alpha_{nuc} = 5 \times 10^{-4}$; the bubble radius $R_B = 1 \times 10^{-6}$; p_v is the saturation vapor pressure; the condensation coefficient $F_{cond} = 0.001$.

To investigate the sabot separation characteristics and the evolution of the surrounding flow field of APFSDS projectiles launched underwater, this paper selects three typical sabot configurations as research objects: the conical sabot, the flat-nosed sabot, and the chamfered leading-edge sabot(Figure 1). The underwater sealed launching method is adopted. At the initial moment, the gun barrel is filled with high-pressure gas, while the exterior is a stationary water domain. During the projectile motion, the CFD equations and the classical interior ballistic equations are solved jointly. These are used to calculate the propulsive force from the propellant gas behind the projectile and the resistance force ahead of the projectile, respectively. At each time step, the fluid resistance ahead of the projectile and the propulsive force behind it are updated synchronously and substituted into the multi-body (sabot and penetrator) DFBI equations to calculate the projectile's trajectory.

At the moment just before the projectile exits the muzzle, the complete in-bore flow field distribution—including pressure, velocity, and temperature—is obtained by solving the interior ballistic equations. This solution is then coupled with the exterior flow field computed via CFD to establish the global flow field state at the instant of muzzle exit. Thereafter, the subsequent evolution of the flow field is entirely governed by the CFD simulation, ultimately providing comprehensive data on the sabot separation process and the associated flow field characteristics during underwater launch.

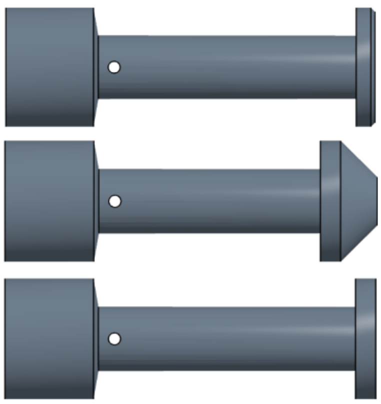

Figure1 sabot configuration

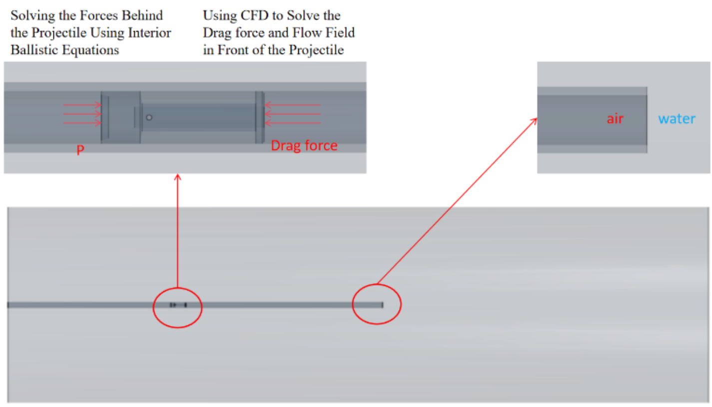

Figure 2 Schematic diagram of the numerical simulation method

3. Result Analysis

To investigate the influencing mechanism of sabot geometry on the separation process of an underwater-launched armor-piercing discarding sabot (APDS) projectile, this study systematically analyzes the underwater launch flow field evolution and motion characteristics under three sabot geometry conditions, with a muzzle velocity of v_0=605.4m/s.

An analysis is conducted on the evolution of the pressure field during the underwater launch process (Figure 3). The separation process of the underwater-launched APDS projectile can be divided into three stages: the Combined motion stage, the mechanical separation stage, and the flow-field separation stage. This separation process is manifested through the evolution characteristics of the pressure field. At t = 0.01 ms, all three types of projectiles have just exited the muzzle. The base of the sabot is subjected to the impact of high-temperature and high-pressure propellant gases, while its nose, as the flow-facing surface, experiences fluid drag. Simultaneously, the projectile is enveloped by a cavitation bubble. Owing to the significant difference in fluid drag between the projectile and the sabot, relative motion between the two has already begun. As the velocity difference between the projectile and the sabot progressively increases, mechanical separation is eventually completed, at which point the projectile is no longer kinematically constrained by the sabot. However, at the instant mechanical separation is completed, the base of the projectile remains within the high-pressure region formed ahead of the sabot, and thus continues to experience hydrodynamic interference. As the projectile and sabot further separate, the projectile gradually escapes from the hydrodynamic influence, marking the end of the APDS separation process and the transition of the projectile into its external ballistic flight phase.

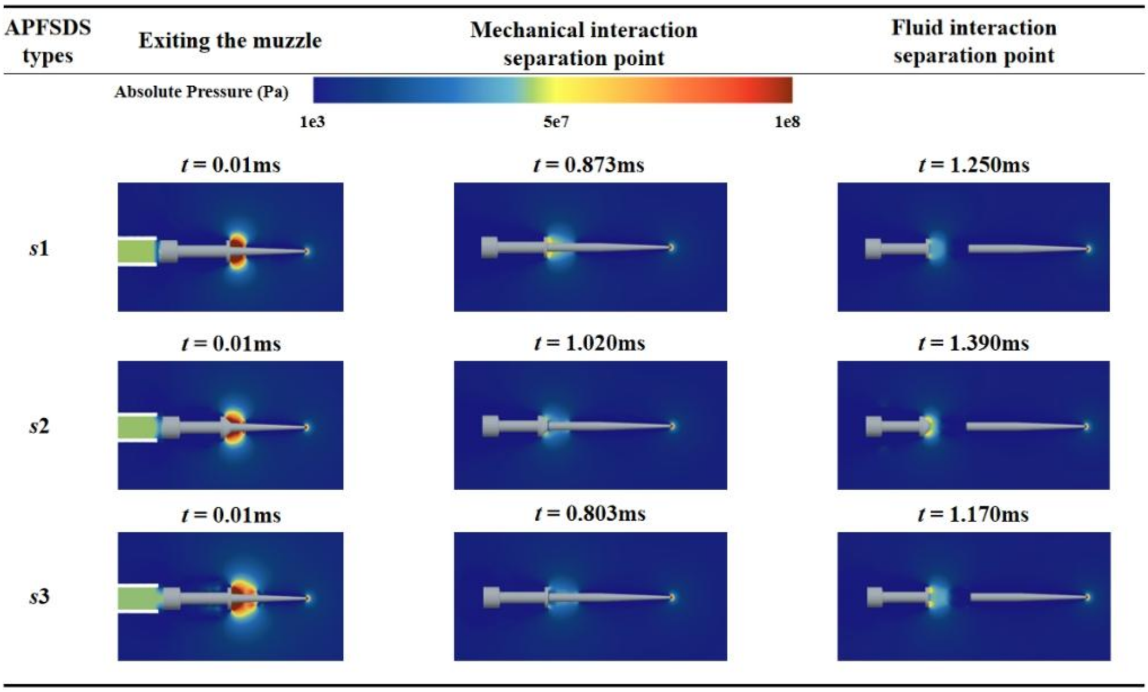

Figure3 Pressure field evolution during the separation process of three armor-piercing discarding sabot (APDS) projectiles.

An analysis is conducted on the evolution of the velocity and temperature fields during the underwater launch process (Figures 4–5). During underwater launch, the pressure and velocity fields can be divided into three distinct regions: the propellant gas region, the flow field around the sabot, and the flow field around the projectile. Throughout the separation process of the armor-piercing discarding sabot (APDS) projectile, the propellant gas continuously expands from the muzzle, resulting in a persistent enlargement of both its velocity and temperature fields. This expansion leads to the formation of a distinctive underwater launch Mach disk structure, which in turn influences the motion of the APDS projectile during the initial stage of separation. Due to differences in the separation timing among the three sabot geometries, the flow field characteristics at the moments of mechanical separation and flow-field separation also exhibit notable variations. In the early stage of APDS separation, the velocity and temperature fields of the projectile and sabot remain coupled: a velocity wake forms downstream of the sabot, while the temperature field around the projectile surface remains relatively low. As the projectile and sabot further separate, the magnitudes of the temperature and velocity fields associated with the sabot gradually diminish. By the moment of flow-field separation, the velocity field at the projectile base has become decoupled from that of the sabot, and the sabot base has moved sufficiently far away from the muzzle Mach disk region.

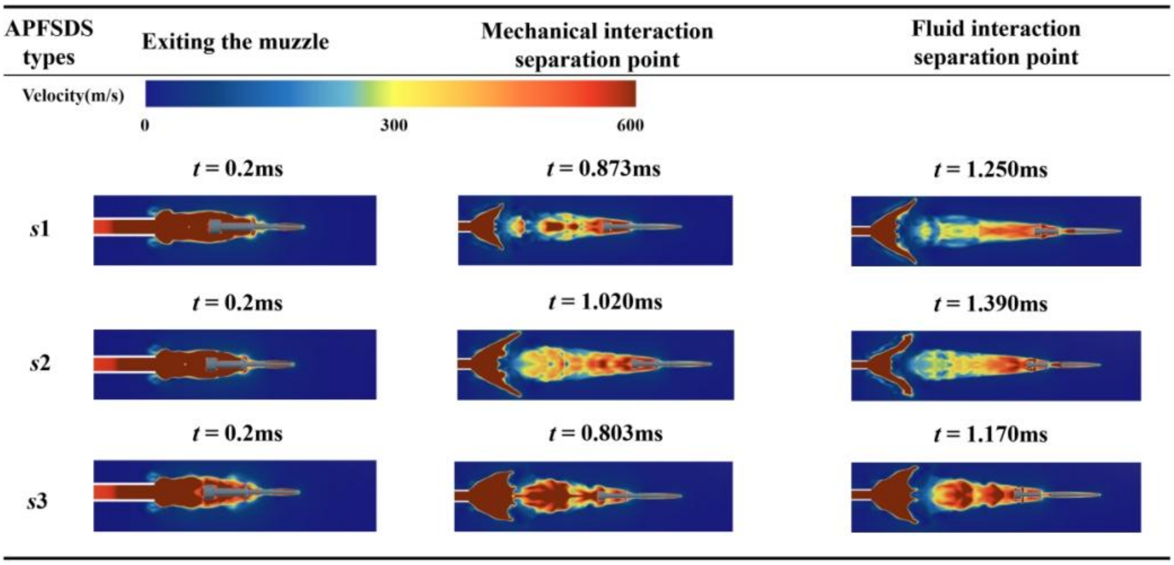

Figure4 Velocity field evolution during the separation process of three armor-piercing discarding sabot (APDS) projectiles.

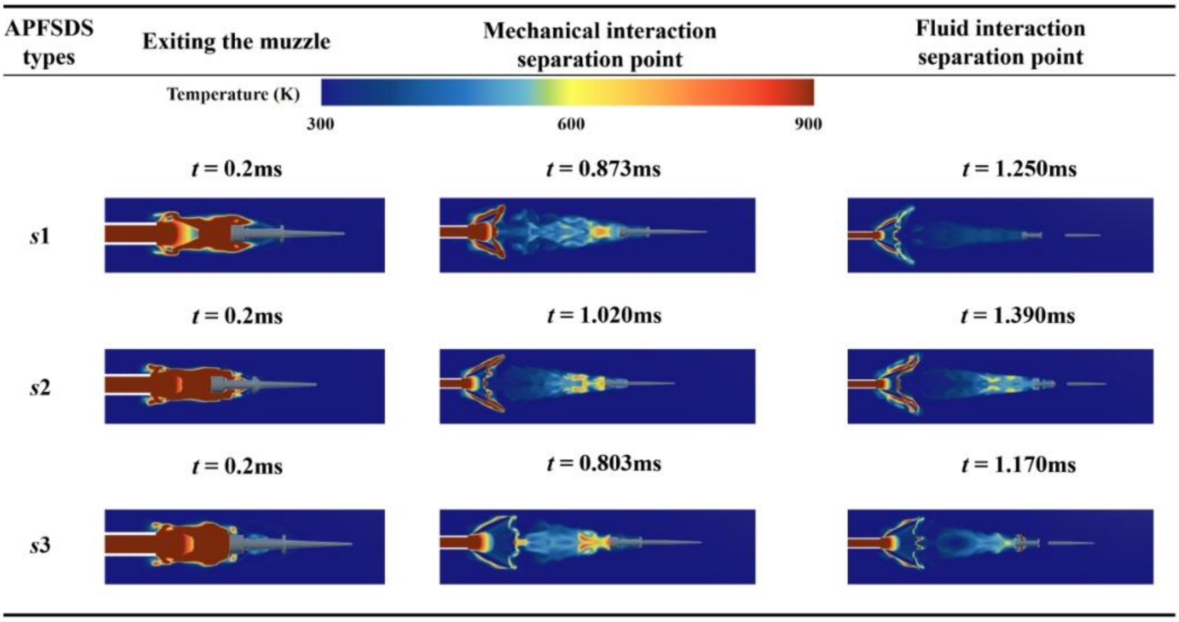

Figure4 Temperature field evolution during the separation process of three armor-piercing discarding sabot (APDS) projectiles.

An analysis of the velocity and displacement variation curves of the projectile and sabot (Figures 6–9) is conducted to reveal the motion characteristics of the two components during the underwater launch and discarding process. From the velocity and displacement curves of the projectile, it can be observed that the displacement differences among the three sabot geometries during the discarding process are relatively small; however, the variations in projectile velocity exhibit distinct differences. At the moment of flow-field separation, the pressure field at the front of the sabot exerts a propulsive effect on the projectile, leading to a brief increase in projectile velocity, after which the projectile velocity further decreases. Regarding the motion characteristics of the sabot, the APDS projectile equipped with the s2-type sabot geometry exhibits the fastest velocity decay, the smallest displacement during the discarding process, and the most gradual separation process.

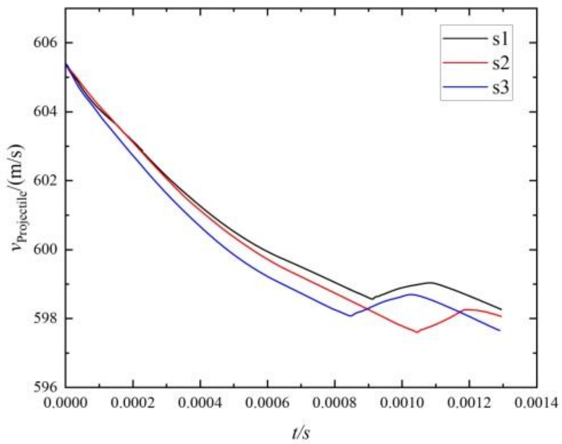

Figure 6 Projectile velocity variation curves for three types of APDS projectiles

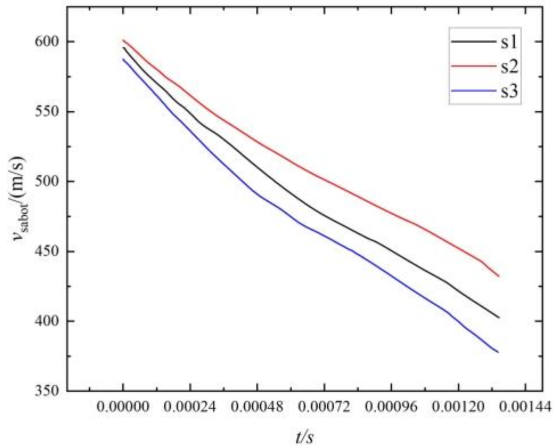

Figure 7 Sabot velocity variation curves for three types of APDS projectiles

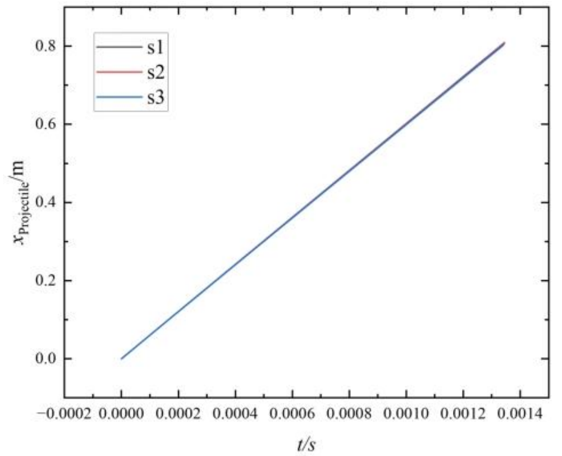

Figure 8 Projectile displacement variation curves for three types of APDS projectiles

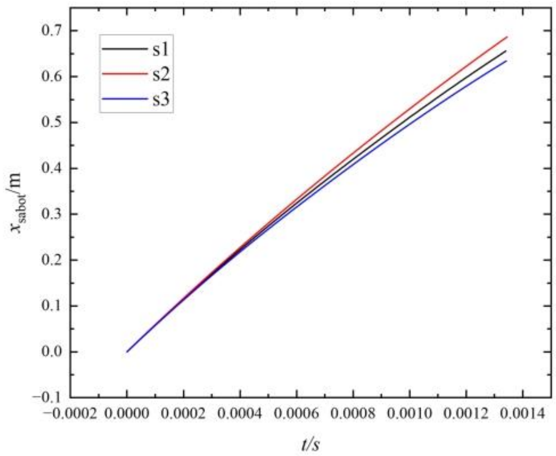

Figure 9 Sabot displacement variation curves for three types of APDS projectiles

An analysis is conducted on the force characteristics of the projectile and sabot during the underwater launch process for APDS projectiles with three different sabot geometries (Figures 10–14). During the discarding process, the cavitation behavior of the three types of APDS projectiles exhibits the following features: the drag on the cavitator and curved surface sections of the projectile shows a decreasing trend as the projectile velocity decreases, albeit with minor fluctuations. The fluid pressure on the cylindrical surface of the projectile, however, first increases and then decreases. The reason for this is that in the early stage of separation, the pressure field at the front of the sabot causes the pressure on the cylindrical surface of the projectile to fall below the cavitation pressure, preventing the formation of a complete cavitation bubble. Consequently, cavitation bubble collapse gradually occurs at the rear end of the projectile's cylindrical surface, leading to a local pressure increase. As the discarding process proceeds, the sabot velocity decreases, the pressure at its front diminishes, and the cylindrical surface of the projectile gradually moves away from the sabot, resulting in a corresponding decrease in pressure in this region. Comparing the forces on the curved and cylindrical sections of the projectile among the three sabot geometries, the s2-type sabot exhibits smaller forces, which is attributed to the distinct pressure field formed at the front surface of this sabot. Overall, the s2-type sabot demonstrates the slowest separation process but exhibits the smallest fluctuations in fluid resistance. Compared with the s1-type and s3-type sabots, the s3-type flat-nosed sabot shows larger force fluctuations on both its own surface and the projectile surface, yet its separation process is faster.

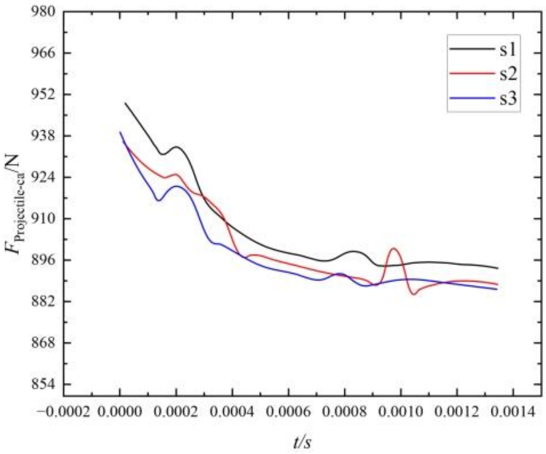

Figure 10 Force curves on the cavitator surface of the projectile for three types of APDS projectiles

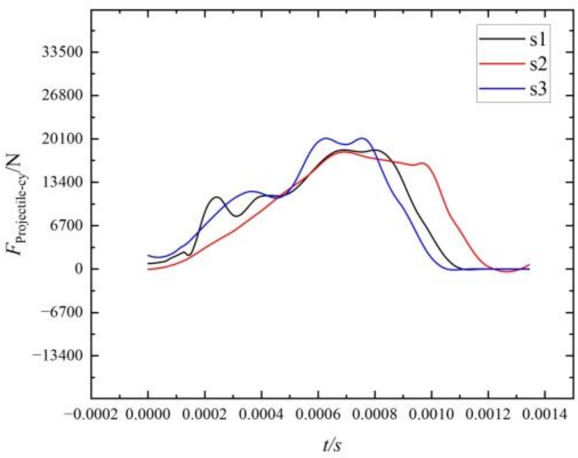

Figure 11 Force variation curves on the cylindrical surface of the projectile for three types of APDS projectiles

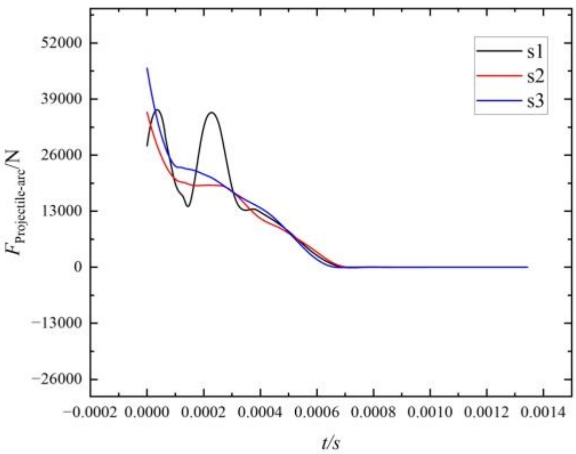

Figure 12 Force curves on the curved surface section of the projectile for three types of APDS projectiles

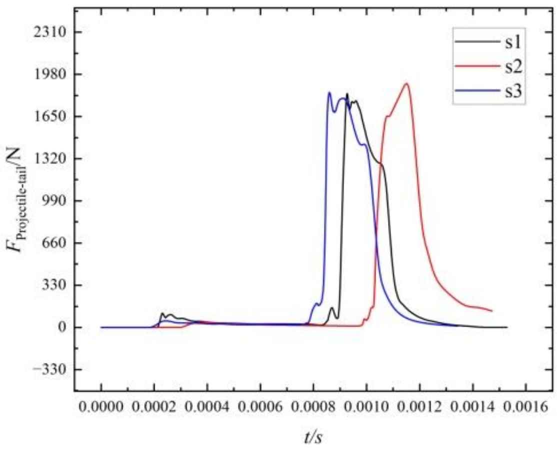

Figure 13 Force curves on the rear end of the projectile for three types of APDS projectiles

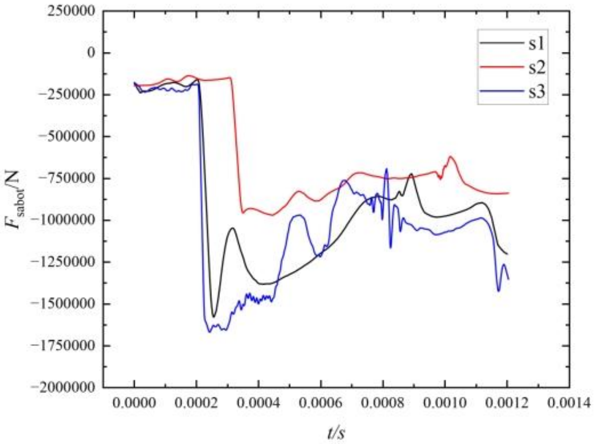

Figure 14 Force curves on the sabot for three types of APDS projectiles

4. Conclusions

This study investigates the sabot configuration of APFSDS projectiles during underwater launch. Three sabot geometries (conical (s2), flat-nosed (s3), and chamfered leading-edge (s1)) are selected as the research subjects. Their hydrodynamic characteristics, flow field distributions, and sabot separation behaviors are systematically analyzed. The main conclusions are drawn as follows:

(1) The underwater launch process of the three types of APFSDS projectiles (s1, s2, s3) exhibits a separation mechanism jointly dominated by mechanical action and fluid action, which differs significantly from the separation behavior of discarding sabot projectiles in traditional air media. The collision between the sabot and the water body marks the initiation of the separation process. At the moment of muzzle exit, the separation behavior has entered the initial development stage. The front end of the sabot and the projectile's cavitator impact the water body at high speed, forming a high-pressure region while simultaneously generating a cavity that envelops the discarding sabot. Concurrently, the rear end of the sabot continues to be propelled by the propellant gas. At the mechanical action separation point, the sabot's motion constraint on the penetrator is released. Notably, at this moment, the tail of the projectile contacts the high-pressure region at the front of the sabot, causing a slight increase in the projectile's velocity. Upon entering the fluid-dominated stage, the cavities and pressure fields of the projectile and sabot gradually separate. The influence of the discarding sabot's flow field on the projectile's motion progressively diminishes until the forces acting on the projectile become completely stable, marking the transition to the external ballistic flight phase.

(2) The conical sabot (s2) exhibits pronounced low-drag characteristics. Due to its streamlined front end, both the mechanical separation point and the hydrodynamic separation point are noticeably delayed, postponing the separation process. However, precisely because of the minimal load borne by its front end, the overall stress on the sabot is uniform and stable, rendering it less susceptible to local buckling or severe deformation. The flat-nosed sabot (s3) achieves an earlier separation response at the cost of an increased frontal area exposed to the flow. Its hydrodynamic separation point is significantly advanced, resulting in a rapid discarding action, which is advantageous for shortening the sabot's disturbance stroke. Nevertheless, the high hydrodynamic pressure acts directly on the frontal plane, readily inducing edge curling and plastic deformation, thereby imposing stricter requirements on the sabot material and structural strength. The chamfered leading-edge sabot (s1) strikes a balance between the two. The chamfered structure mitigates the peak resistance at the front end to a certain degree, causing its separation point to be slightly later than that of the flat-nosed sabot but still significantly earlier than that of the conical sabot. Simultaneously, the chamfered edges effectively alleviate local stress concentration caused by flow separation. Furthermore, its velocity attenuation is the smallest among the three sabot types, making it an effective compromise solution that balances separation rapidity with structural reliability.

Acknowledgements

The present work are financially supported by the Fundamental Research Funds for the Central Universities,(No.30925010417， No.30925020220)and National Natural Science Foundation of China Youth Fund(52301374).

References

[1] Zeqing G, Xuepu Y, Shuai S, et al. Experimental study on the high-speed water entry of cylinders at shallow angles[J]. Physics of Fluids, 2024, 36(10): 104123.

[2] Xuan Z ,Yonggang Y ,Xinwei Z .Numerical simulation and analysis of the 3D transient muzzle flow field of underwater artillery[J].Ocean Engineering,2023,284.

[3] Panda S S ,Gite L ,Anandaraj A , et al.Dispersion sensitivity analysis & consistency improvement of APFSDS[J].Defence Technology,2017,13(4):316-322.

[4] Acharya R, Naik S. Perturbation of Initial Stability of an FSAPDS Projectile[J]. Defence Science Journal, 2006, 56(5): 753-768.

[5] Acharya R ,Naik S. Motion analysis during sabot opening process[J]. Defence Science Journal, 2007, 57(2): 229-241.

[6] Chengqing Z ,Huiyuan W ,Ting L , et al.Sabot Discard Characteristics under Different Spin Rates of the Rifled Barrel Launching APFSDS[J].Shock and Vibration,2021.

[7] Huang Z ,Xia C ,Cao Y , et al.Numerical investigations on the sabots discard process of an APFSDS at different angles of attack[J].The Journal of Engineering,2019,2019(13):373-378.